MAPb(Br1–xClx)3 Hybrid Perovskite Materials for Direct X-ray Detection

Javier Mayén Guillén, Ferdinand Lédée, Oriane Baussens, Marian Chapran, Thibault Lemercier, Jean-Marie Verilhac, Eric Gros-Daillon, Alain Ibanez, Julien Zaccaro

To cite this version:

Javier Mayén Guillén, Ferdinand Lédée, Oriane Baussens, Marian Chapran, Thibault Lemercier, et al.. MAPb(Br1–xClx)3 Hybrid Perovskite Materials for Direct X-ray Detection. ACS Applied Electronic Materials, 2023, 5 (3), pp.1866-1878. 10.1021/acsaelm.3c00114 . hal-04021522

HAL Id: hal-04021522
https://cnrs.hal.science/hal-04021522

Submitted on 29 Mar 2023

$MAPb(Br_{1-x}Cl_x)_3$ hybrid perovskite materials for direct X-ray detection

Journal:	*ACS Applied Electronic Materials*
Manuscript ID	el-2023-00114t.R2
Manuscript Type:	Article
Date Submitted by the Author:	n/a
Complete List of Authors:	Mayén Guillén, Javier; CEA LITEN Lédée, Ferdinand; CEA-Leti Baussens, Oriane; CEA-Leti Chapran, Marian; CEA-Leti Lemercier, Thibault; Institut NÉEL Verilhac, Jean-Marie; CEA LITEN Gros-Daillon, Eric; CEA-Leti Ibanez, Alain; Institut NÉEL Zaccaro, Julien; Institut NÉEL

$MAPb(Br_{1-x}Cl_x)_3$ hybrid perovskite materials for direct X-ray detection

Javier Mayén Guillén [a], Ferdinand Lédée [b]*, Oriane Baussens [b], Marian Chapran [b], Thibault Lemercier [c], Jean-Marie Verilhac [a], Eric Gros Daillon [b], Alain Ibanez [c], Julien Zaccaro [c]*

[a] Grenoble Alpes University, CEA, LITEN, DTNM, F38000 Grenoble, France

[b] Grenoble Alpes University, CEA, LETI, DOPT, F38000 Grenoble, France

[c] Grenoble Alpes University, CNRS, Grenoble INP, Institut Néel, F38042 Grenoble, France

*Email: javier-alejandro.mayenguillen@cea.fr; ferdinand.ledee@cea.fr

KEYWORDS: anion engineering, halide, doping, optoelectronic performance, hybrid perovskite, single crystal, X-ray detection

ABSTRACT: The study and development in recent years of hybrid (organic-inorganic) halide perovskite materials make them an unprecedented opportunity for direct ionizing radiation detection, given their large attenuation coefficient and sufficient charge carrier mobility-lifetime product. The use of single crystals, considered as model materials, allows us to investigate their intrinsic properties. Characterizations under X-ray illumination of detector devices based on methylammonium lead tribromide ($MAPbBr_3$) single crystals, obtained by optimized-growths, show good sensitivity but high dark current density. To improve this critical parameter, while using $MAPbBr_3$ as base material, we employ anion engineering within the halide elements. We present here mixed halide perovskite crystals, with bromide partially replaced with chloride, obtained through optimized-growths using Modified Inverse Temperature Crystallization in dimethylformamide, leading to high quality single crystals of general formula $MAPb(Br_{1-x}Cl_x)_3$. Six chlorine contents are targeted and carefully determined experimentally via Energy dispersive X-ray analysis and X-ray powder diffraction. For each composition, several crystals are synthesized and used to prepare X-ray detection devices. Their optoelectronic properties are determined under standard X-ray medical conditions and hint at the existence of an optimal composition. $MAPb(Br_{0.85}Cl_{0.15})_3$ exhibits the best sensitivity with a value of $S \approx 3\ \mu C\ mGy_{air}^{-1}\ cm^{-2}$ for RQA5 spectral quality and the lowest dark current density with a value of $J_{dark} \approx 22\ nA\ mm^{-2}$, both recorded at a $50\ V\ mm^{-1}$ electric field. This sensitivity value doubles our own $MAPbBr_3$ single crystal device and is higher than that of CsI(Tl) - or a-Se-based flat panels. The present work broadens the benefits and drawbacks of employing halide engineering in perovskite materials to improve optoelectronic performance under high-energy radiation.

1. INTRODUCTION

The strong penetrating capability of high-energy ionizing radiation (X- and γ-rays) is attractive for non-destructive probing of condensed matter. In medical imaging, the sensing of the ionizing radiation signal that has interacted with the human body can be done indirectly or directly. The former employs a scintillator, converting high-energy photons into ultraviolet-visible light (e.g. CsI(Tl), NaI(Tl)) and in turn photodiodes, converting that light into electric signal. The latter uses a semiconductor layer that directly converts the incoming photons into electron-hole pairs that become charge carriers collected thanks to the presence of an electric field (e.g. α-Se, HgI_2, $Cd_{1-x}Zn_xTe$ (CZT)).

Direct detectors for high-energy photons require semiconducting materials with a thickness and linear attenuation coefficient large enough to efficiently absorb most of the incoming radiation, large and balanced charge carrier mobility (μ) - lifetime (τ) product (μτ product) for efficient charge collection, high resistivity ρ and low charge trap density to avoid charge trapping and decrease signal noise.[1,2] During the last decade, halide based perovskite materials have generated strong and growing attention for being promising candidates for optoelectronic applications, and in particular for high-energy radiation detection. Indeed, hybrid (organic-inorganic) halide perovskite materials show good X-ray absorption, thanks to the presence of heavy elements such as lead,[3–5] a defect tolerant nature,[3,6,7] sufficient μτ product,[8] and simple crystal growth from solution.[9,10] Therefore, heavy metal halide perovskites are well suited for direct X-ray detection applications like medical imaging.[11] Additionally, these materials, in the form of single-crystals (SC), exhibit no grain boundaries and possess very low trap densities.[2,3,6,7,12] From a fundamental point of view, working with SCs is the most favorable way to directly access their intrinsic bulk properties which is critical to identify the best compounds for practical applications.

Methylammonium lead tribromide ($MAPbBr_3$) is among the most studied hybrid halide perovskites for high-energy radiation detection,[3,4,13] being more stable than its iodide-based counterpart, methylammonium lead triiodide ($MAPbI_3$).[14] Within our team, $MAPbBr_3$ SCs growth via Modified Inverse Temperature Crystallization (MITC) has been optimized in dimethylformamide (DMF) for direct X-ray radiation detection.[11,15] Their optoelectronic properties have been evaluated under X-ray illumination and while the growth optimization allowed reaching a very good sensitivity, they always presented a large dark current density

J_{dark} (~ µA cm^{-2}), being several orders of magnitude above the specifications required for radiation detectors.[16] This crucial figure of merit for detectors corresponds to the leakage current of the device in the dark, and must be minimized by a combination of increased bulk resistivity ρ and electrode engineering.[17,18]

In this context, to reduce the dark current, it has been recently proposed to modify the bulk chemical composition of $MAPbBr_3$ by partially substituting bromine with chlorine leading to compounds of general formula $MAPb(Br_{1-x}Cl_x)_3$.[19] According to several studies, this anion engineering would lead to higher bulk resistivity ρ, increased charge carrier mobility μ and lifetime τ, and lower hysteresis compared to base material.[2,19–22] However, the origin of those improvements remains unclear. On the one hand, Rybin et al.[19] and Wang et al.[22] attributed the improvements to the suppression of Br^- anions migration induced by lattice contraction and decrease in halide vacancy, while on the other hand, Wei et al.[2] proposed a dopant compensation mechanism as the source of electronic neutrality and subsequent increased resistivity. This discrepancy could be explained by considering that the different studies were based on crystals made by different methods and therefore with different dominating defect structures. $MAPbBr_3$ can present different crystal quality depending on the growth method employed, as it has been observed in photovoltaics.[23] As a result, the halide substitution had different impacts, either mostly electronic, structural or a mixture of both, depending on the case. Furthermore, we notice that the above mentioned studies draw different conclusions regarding the performance dependency on the Cl-composition: no consensus on the optimal Cl content is established.

If defects are the key in understanding Cl addition effect, then specific attention should be given to crystal growth to ensure that the defect structures are comparable between crystals. Most studies cited above relay on spontaneous nucleation as the initial stage of crystal synthesis. While this can lead to high quality crystals, we have observed that it yields crystals with a large diversity in defect content (dislocation density, strains) and properties.[15] Also, in many of these studies mixed halide crystals are grown in DMF/DMSO (dimethyl sulfoxide) mixtures of varying proportions.[20,22] While it makes sense to compensate the lower solubility of species with chloride in DMF by increasing the DMSO proportion with increasing Cl content, it could have an adverse effect on the grown crystals properties as it has been claimed that DMSO favors the formation of defects (MA^+ vacancies V_{MA}) in $MAPbBr_3$ when it is used in large proportion (> 3 %).[24]

While the performance of $MAPb(Br_{1-x}Cl_x)_3$ SCs has largely been assessed for γ-ray detection,[2,4,19,25] its performance as X-ray detector, and specially for radiography applications has been seldom reported.[2,26] To contribute to the understanding of the impact of Cl incorporation in $MAPbBr_3$, we present here a study on the properties of mixed halide $MAPb(Br_{1-x}Cl_x)_3$ SCs, grown by our method and supported by significant device sampling per composition. Their performance was assessed under standard X-ray medical conditions, representing an unexplored path for important applications (e.g. medical radiography, mammography, dosimetry). The crystal growth took place in DMF, from seeds and under conditions similar to the ones we have previously used, leading to crystal with low and reproducible defect content.[15] In that sense, if an optimal Cl content was identified, it could not be argued that it resulted from an adverse effect of DMSO or the crystal growth technique but solely from the presence of Cl in the structure. Different solution Cl contents were selected in the range where optimal properties have been previously identified, namely $\%Cl_{sol} = 0, 1, 2, 5, 10$ and 100. For each content, compositional, optical and electrical characterizations of the resulting SCs were systematically undertaken to evaluate the crystals properties. Energy dispersive X-ray analysis (EDX) via field emission scanning electron microscopy (FESEM), and X-ray powder diffraction (XRD) allowed to determine the Cl content inside the crystal lattice ($\%Cl_{cryst}$) and cell parameter a. The optical band gap E_g, via ultraviolet (UV)-visible spectroscopy, and steady-state photoluminescence (PL) as a function of Cl content were determined. After crystal polishing and Cr electrodes deposition, the optoelectronic performance of each composition was evaluated via current density-voltage (J-V) sweeps, current density-time (J-t) and laser time of flight (ToF) measurements, and response under X-ray radiation (sensitivity-voltage (S-V) measurements) in relevant medical imaging conditions (pulsed X-rays at 4 Hz, 100 ms pulse duration, 24 μGy_{air} per pulse RQA5 quality beam corresponding to an angiography exam). S-V data were subsequently modeled using two-charge carriers Hecht equation for evaluation of $\mu\tau$ product. The crystal growth method and characterization conditions lead to the existence of an optimum in Cl content.

2. RESULTS AND DISCUSSION

2.1. Substitution of Br with Cl

Cl-containing SCs were grown via a MITC method similar to the one described in previous work for $MAPbBr_3$ (see Figure S1 in Supporting Information).[15] One of its key element is that it employs a seed-assisted growth. Because of its inherently stochastic nature, spontaneous nucleation may give rise to crystals of varying quality with extended defects such as grains boundaries, strains or dislocations, which make the comparison between crystals of a given composition less straightforward and may induce different actions of Cl^- anions in the structure. To ensure comparability, the crystals of all compositions were grown from seeds of similar quality. For each selected $\%Cl_{sol}$, during a first growth run, seeds of matching composition were obtained by spontaneous nucleation. The best of them, well faceted SCs and free from internal strains, were then used in a second seed-assisted crystal growth run in a solution of same Cl content, to obtain reproducible quality SCs of bigger dimensions for this study (for more details, see the Experimental Section and Supporting Information). As indicated above, the selected Cl contents in solution were $\%Cl_{sol}$ = 0, 1, 2, 5, 10 and 100. Because Cl-containing precursors are sparingly soluble in DMF,[27] we introduced chloride via the most soluble one, MACl. The lower solubility of Cl-species also impact the growth conditions as it leads to a global lower solubility and slightly lower solubility-temperature ratios of mixed halide perovskite with increasing Cl content (see Figure S2 for solubility curves of $MAPbBr_3$ and $\%Cl_{sol}$ = 10 ($MAPb(Br_{0.85}Cl_{0.15})_3$) in DMF). To accommodate these changes, different temperatures ramps were employed. On the one hand, the temperature ramp of 5.5 °C h^{-1} used for $MAPbBr_3$ and $\%Cl_{sol}$ = 1 was reduced by a factor of about 5 for $\%Cl_{sol}$ = 2, 5, 10 (1°C h^{-1}). On the other hand, for $MAPbCl_3$ ($\%Cl_{sol}$ = 100), as the growth cannot be carried out in pure DMF, a DMF/DMSO mixture (3:7 in volume) was used with a ramp of 1.6 °C h^{-1}.[20] The reduction of the temperature ramp (1/5) was more important than that of the solubility-temperature ratio (1/2) to ensure that the solution stays in the reduced metastable zone and avoid significant spontaneous nucleation in Cl-rich solutions. It is because nucleation would become predominant in growth conditions used for $MAPbBr_3$ that we limited our study to rather low Cl contents, in order to grow mm-sized crystals of different Cl contents but under similar growth conditions. Additionally, it has been observed that Cl concentration above %Cl = 19 ($MAPb(Br_{0.81}Cl_{0.19})_3$) may induce detrimental defects.[28] Ultimately, a total of 51 crystals of 4 mm × 4 mm × 2 mm on average were grown during this work to provide sufficient statistical weight to the characterizations (see Figure S3).

Our first task was to determine the amount of Cl in the crystals. In general, through various physical-chemical phenomena such as differences in speciation, complexation and diffusion, the amount of substituent incorporated in the crystal (denoted here $\%Cl_{cryst}$) differs from the one put in solution ($\%Cl_{sol}$). For that reason, for each composition, the crystals Cl content was determined using two independent techniques, EDX and XRD.

EDX spectra were recorded using a Zeiss Ultra+ FESEM on flat natural faces of several crystals grown from each solution composition (see Experimental Section and Supporting Information).

Examples of resulting spectra are overlaid in Figure 1A showing only a narrow energy range centered on the Cl K_α emission line (full range EDX spectra can be found in Figure S4). The most striking feature is the expected progressive rise of Cl^- anions in the crystal (from red to light green lines) with increasing $\%Cl_{sol}$ (see Supporting Information for quantification details). Plotting the Cl concentrations in the crystal derived from these EDX measurements ($\%Cl_{cryst\text{-}EDX}$) against the ones in solution $\%Cl_{sol}$ (green plot in Figures 1B and 1C) shows an efficient incorporation of Cl^- anions in the crystal structure with a partition coefficient k higher than unity ($\%Cl_{cryst} > \%Cl_{sol}$). A possible explanation of the partition coefficient being above unity, could derive from the lower solubility of Cl-species as evidenced by the lower solubility of $MAPbCl_3$ precursors in DMF when compared to that of $MAPbBr_3$.[27] One can then assume that chloroplumbate complexes present in the precursors solution would precipitate faster and contribute more to the structure build-up than bromoplumbate ones. As a consequence, during crystal growth, Cl-enriched perovskite is initially deposited and the solution becomes progressively poorer in Cl. This drift in Cl content in solution can result in significant compositional heterogeneity between the inner/early growth and the outer/late growth parts of large SCs. To quantify such heterogeneity in our crystals, SCs were cleaved and a profile study by EDX was performed for $\%Cl_{sol} = 2$ and 5, to try and see any evolution of Cl content in the crystal thickness. The corresponding SEM pictures and respective EDX measurements are available in Figures S5 and S6, respectively. For $\%Cl_{sol} = 2$, due to the level of uncertainty of EDX measurements and surface microtopography heterogeneity of the crystal (Figures S5-A and S6-A), no clear trend was observed. For $\%Cl_{sol} = 5$, on the contrary, a decreasing Cl content can be observed, going from 8.2 ± 0.6 % close to the seed (bottom) of the crystal to 6.5 ± 0.6 % for later growth (top) (Figures S5-B and S6-A). The EDX analysis is localized to the beam size and only sensitive to the top few micrometers. Because the late growth of the crystal occurs in the solution most depleted in Cl from the initial ratio $\%Cl_{sol}$, the Cl content values of the crystals estimated by EDX probably underestimate the average Cl content of the whole bulk crystal. That is why, to precisely estimate the average Cl content of the crystals grown in solution, we relayed on XRD.

Indeed, another way to estimate the average Cl content of the crystals is through its impact on the unit cell parameter. XRD data were recorded for all compositions on grinded crystals (Figure S7) so that whole volume of the crystals contribute to the measurement. The diffractions patterns showed small peak shifts toward higher angles with increasing Cl content (Figures S7 and S8), associated with a contraction of the unit cell. This contraction is related to the substitution of Br^- by Cl^- anions of smaller ionic radius (r_{Cl^-} (1.81 Å) < r_{Br^-} (1.92 Å)) and consequently shorter length of Pb−Cl than Pb−Br bonds.[19] All studied compositions appear isomorphous with the existence of a continuous solid solution between $MAPbBr_3$ and $MAPbCl_3$. So, the unit cell parameter is expected to follow a Vegard's law (VL) (Equation S7) as a function of the Cl content. By performing Le Bail refinements of diffractograms from crystals grown in each mixed halide solution composition as well as pure $MAPbBr_3$ and $MAPbCl_3$, lattice parameters *a* were precisely determined (see Table S6). Reliability factors for points with Bragg contributions are shown in Table S2. By applying the VL based on the cell parameters of the pure phases, average Cl content of the crystals $\%Cl_{cryst\text{-}XRD}$ were calculated. In Figure 1C, the resulting values are plotted as a function of the Cl solution content (blue line), confirming that the Cl partition coefficient k is higher than unity and $\%Cl_{cryst\text{-}EDX}$ values. Because XRD gives an estimation that is more precise as well as based on the whole volume of the crystals, the $\%Cl_{cryst\text{-}XRD}$ values were considered to be more representative and are the ones used in the rest of this manuscript to define our crystals Cl content, $\%Cl_{cryst\text{-}XRD}$ being shortened to $\%Cl_{cryst}$ (see Table S1 for overall values). The resulting material compositions are then: $MAPbBr_3$, $MAPb(Br_{0.98}Cl_{0.02})_3$, $MAPb(Br_{0.97}Cl_{0.03})_3$, $MAPb(Br_{0.92}Cl_{0.08})_3$, $MAPb(Br_{0.85}Cl_{0.15})_3$ and $MAPbCl_3$, corresponding to $\%Cl_{sol}$ = 0, 1, 2, 5, 10 and 100, respectively.

Beyond the Cl content and its homogeneity in the crystals, these measurements can also shed some light on the lead-halogen (Pb-X) stoichiometry which is correlated with the point defects present. By using the EDX measurements presented above, one can estimate local values of the Pb/X ratio for the different synthesized crystals and also within the same SCs. Between crystals of different composition, it appears that Pb/X ratio gets closer to ABX_3 stoichiometry (33.3%) with increasing Cl incorporation (Figure 1B): raising from 28.5 ± 0.4 % for $MAPbBr_3$ to 30.5 ± 1.3 % for $MAPb(Br_{0.85}Cl_{0.15})_3$, while $MAPbCl_3$ has a Pb/X ratio of 34.3 ± 0.9 %. Now regarding the Pb/X ratio of the profile study, within the $MAPb(Br_{0.92}Cl_{0.08})_3$ SC, the same tendency was observed. That is to say a Pb/X value closer to the stoichiometry was observed for the early stages of the crystal growth (richer in Cl at the seed side), decreasing for the later growth (poorer in Cl) (see Figures S6-B). This highlighting that the compositional heterogeneity is not a simple Br-Cl substitution, but also impacts the stoichiometry of the structure, moving away from a “Pb poor” situation with Cl incorporation. This shift of the Pb-X stoichiometry, accompanying the Cl incorporation may be attributed to a decrease in lead vacancies V_{Pb}, or conversely an increase in interstitial halide X_i or halide antisite X_{Pb}. EDX measurements were limited to a depth inferior to 900 nm that this why Inductively Coupled Plasma Mass Spectrometry (ICP-MS) measurements, involving the whole SC, were additionally done for bulk composition analysis (see Table S3) to complement surface versus bulk Pb/X ratio trends in $MAPbBr_3$. The results showed that, at the SC level, the 33.3% stoichiometry is already present for pure bromide samples, meaning that we are dealing with local Pb/X ratio modifications. These results are correlated with optoelectronic properties further on in the Discussion.

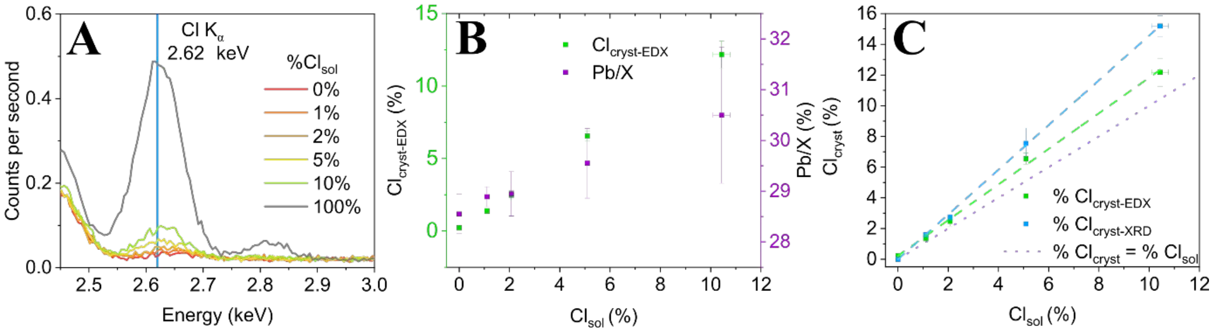

Figure 1. Substitution of Br$^-$ by Cl$^-$ anions. (A) EDX spectra overlaid centered on Cl K$_\alpha$ (2.62 keV) emission line to show progressive and preferential substitution of Br$^-$ with Cl$^-$ anions. From bottom to top: $MAPbBr_3$, $MAPb(Br_{0.98}Cl_{0.02})_3$, $MAPb(Br_{0.97}Cl_{0.03})_3$, $MAPb(Br_{0.92}Cl_{0.08})_3$, $MAPb(Br_{0.85}Cl_{0.15})_3$ and $MAPbCl_3$. **(B)** Correlation between solution Cl content %Cl$_{sol}$ and both crystal Cl content %Cl$_{cryst-EDX}$ (green squares) and Pb/ halide ratio (Pb/X) (purple squares) determined by EDX respectively. Reference $MAPbBr_3$ and mix halide compositions are plotted. **(C)** Correlation between solution Cl content %Cl$_{sol}$ and both crystal Cl contents %Cl$_{cryst-EDX}$ and %Cl$_{cryst-XRD}$ determined by EDX (green squares and dot line) and Vegard's law (VL) from XRD data (blue squares and dot line), respectively. Unity (k = 1) is displayed with purple dots (%Cl$_{cryst}$ = %Cl$_{sol}$). Both crystal Cl contents are higher than unity showing a progressive Cl-impoverishment of solution and the synthesis of Cl-enriched SCs.

2.2 Optoelectronic properties and performances of $MAPb(Br_{1-x}Cl_x)_3$ SCs

Replacing Br by Cl not only induces a contraction of the unit cell but also a visible change of the crystal color with increasing Cl content (seen in Figure 2A) which is a clear indication of change in optical band gap. To quantify this change, the optical band gaps E_g were determined via UV-visible spectroscopy. Transmission data (T(%)) show a gradual blue shift in absorption onset (Figure 2B). The band gap values extracted from the corresponding Tauc plots (Figure S9) are plotted as a function of $\%Cl_{cryst}$ in Figure 2C, showing a linear increase of E_g with rising Cl content for the considered range. Steady-state photoluminescence (PL) spectra, in Figure S10, displays also a gradual blue shift of excitation PL maxima, corroborating the E_g increase determined by the Tauc plots.

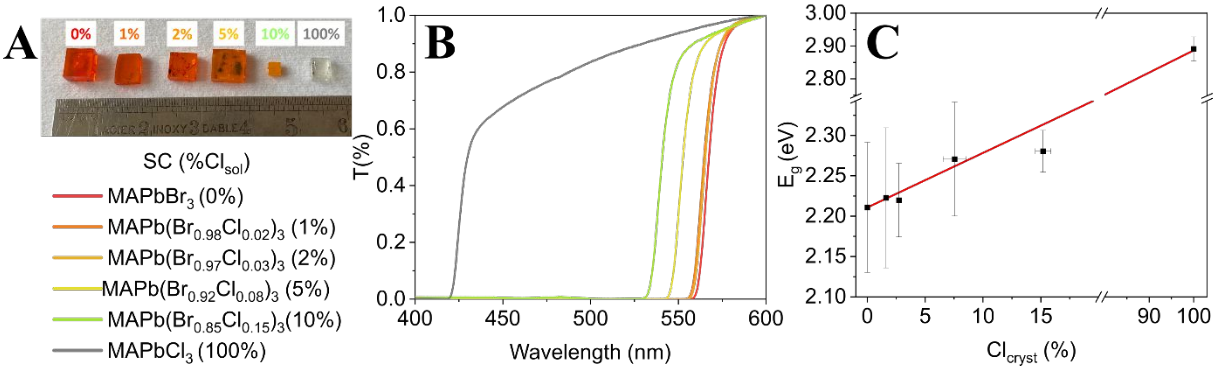

Figure 2. Optical properties of $MAPb(Br_{1-x}Cl_x)_3$ SCs. (A) Resulting SCs (from left to right): $MAPbBr_3$, $MAPb(Br_{0.98}Cl_{0.02})_3$, $MAPb(Br_{0.97}Cl_{0.03})_3$, $MAPb(Br_{0.92}Cl_{0.08})_3$, $MAPb(Br_{0.85}Cl_{0.15})_3$ and $MAPbCl_3$ (targeted $\%Cl_{sol}$ written in color above each SC). The Cl content in the formulae is the one determined via the Vegard's law (VL) from XRD data as shown in the legend below. **(B)** Transmittance spectra overlaid showing gradual absorption transition blue shift with increasing Cl content, synonym of increasing optical band gap E_g. **(C)** Optical band gap E_g of resulting SCs as a function of crystal Cl content $\%Cl_{cryst}$.

Among the 51 crystals grown in this work, around one half was dedicated to physicochemical characterizations. The other half (24 crystals) were used to make optoelectronic devices by polishing and depositing Cr electrodes on both sides (see Experimental Section and Supporting Information). The results discussed below are extracted from the measurements performed on four different series, containing each an exemplary of every composition. From 2 to 4 SCs per composition were evaluated, depending on the characterization technique (J-V, J-t, sensitivity and ToF measurements). Figure S3 shows the resulting devices with their respective thicknesses in inset.

Globally, J-V sweeps of all devices do not exhibit any significant hysteresis whatever the composition, with or without chloride: see Figure 3A-1 for J-V sweeps example on a single series and Figures S11 to S14 for all evaluated series. Such hysteresis feature is commonly attributed to mechanisms induced by ion migration under non-equilibrium conditions.[29] Previous studies reported a hysteresis decrease for $MAPb(Br_{1-x}Cl_x)_3$ compositions compared to the pure bromide one.[19,22] They favored a structural approach to this ion migration, by considering that the unit cell contraction and the distortions induced by the presence of Cl inside the crystal lattice would reduce Br^- anions migration and consequently stabilizing the current density under large electric field.[19] In our case, the reference $MAPbBr_3$ samples are already free from hysteresis and so do not benefit from such positive effect related to Cl addition.

Regarding dark current density versus time (J-t) measurements in the dark, the SC devices showed stable signal over time. A section of the measurements is shown in Figure 3A-2. For an evaluation time of 10 min, $MAPbBr_3$ showed a conductivity drift σ_{drift} (defined by Equation S12) of 7.9×10^{-4} S m^{-1} s^{-1}, which gradually decreased with increasing Cl content, reaching a minimal value for $MAPb(Br_{0.85}Cl_{0.15})_3$ with 2.9×10^{-4} S m^{-1} s^{-1}, both values corresponding to 4.7 % and 3.8 % of initial dark current drift under 50 V mm^{-1}, respectively (see Supplementary

Information for further details). This may be potentially linked to the close to nominal composition of this material in terms of Pb/X ratio, as shown in the previous part. All compositions drifts were lower than what was previously reported in the literature (see Table S4 for all compositions σ_{drift} values).[2]

Resistivity values were extracted from the J-V sweeps in the ohmic region reaching an average value of $\rho_{avg} = 1.1 \times 10^8$ Ω cm for $MAPbBr_3$, the crystals with mixed halide composition being in the same order of magnitude with the exception of $MAPbCl_3$ which is significantly less resistive ($\rho_{avg} = 2.9 \times 10^7$ Ω cm) as showed in Figure 3B-1. In the present work, we found that the addition of small amounts of chloride during crystal growth does not improve the resistivity as oppositely demonstrated by Wei et al.[2] for $MAPb(Br_{0.98}Cl_{0.02})_3$ SC and Rybin et al.[19] for $MAPb(Br_{0.95}Cl_{0.05})_3$ reaching resistivities of 3.60×10^9 Ω cm and $1.522 \pm 0.156 \times 10^9$ Ω cm, respectively. In both studies the increase of resistivity with optimal chloride compositions is 5 times above their reference $MAPbBr_3$ samples. A dopant compensation mechanistic approach has been proposed to explain the benefits of adding Cl in $MAPbBr_3$ by considering it intrinsically a p-type semiconductor due to lead vacancies V_{Pb} and $MAPbCl_3$ intrinsically a n-type semiconductor due to halide vacancies V_X.[2]

It is important at this point to define the term “doping” which is broadly used in halide perovskites literature to describe the introduction of any kind of impurity into the crystal lattice to control growth, stability and/or tune optoelectronic properties.[30,31] We refer to electrical doping when an impurity or defect generates free carriers or shifts the Fermi level,[32] which is the case in Wei et al. work.[2] This doping relies on the formation of intrinsic (vacancies, interstitials or site substitutions) and/or extrinsic (impurities) defects. In the case of $MAPbBr_3$, Shi et al. showed a predominantly unipolar self-doping character, with a tuning range from degenerately p-doped under Br-rich and Pb-poor condition to intrinsic or slightly n-doped in Br-poor and Pb-rich condition.[33] According to EDX data (Figure 1B), in our case, we are dealing with a “thermal equilibrium grown” Br-rich and Pb-poor $MAPbBr_3$ SC, with a Pb/Br ratio of 28.5 ± 0.4 % (which would point to V_{Pb} as predominant, thus p-doped) and a Cl-poor and Pb-rich $MAPbCl_3$ SC, with a Pb/Cl ratio of 34.3 ± 0.9 % (V_X predominant, thus n-doped). Stoichiometry is progressively reached with increasing Cl content, being the closest to it with a Pb/X value of 30.5 ± 1.3 % for $MAPb(Br_{0.85}Cl_{0.15})_3$ (similar population proportion then for both V_{Pb} and V_X).

One would expect then a dopant compensation in our SCs, but the above mentioned improvements were not seen in this study for both hysteresis and resistivity, even though our SCs are in the considered optimal range %Cl ≈ 2 - 17 ($MAPb(Br_{0.98}Cl_{0.02})_3$ - $MAPb(Br_{0.83}Cl_{0.17})_3$).[2,19,22] The difference in behavior with the literature could be partially explained by the initial type of doping of $MAPbBr_3$ material and associated defect structures. Experimental conditions leading to an n-type $MAPbBr_3$ reference would explain why addition of Cl do not have a significant impact on the resistivity. In that case, the n-type self-compensation brought by Cl would be inefficient. By taking into consideration just intrinsic defect doping, we could consider to control the initial doping by tuning the precursors ratio PbX_2/AX in $APbX_3$, *A* being any cation forming a 3D structure. Despite a few experimental examples managing a transition from p-type to n-type for $MAPbI_3$ and $FAPbI_3$ (FA = formamidinium),[34,35] just one transition from p-type to n-type with increasing $PbBr_2$/MABr ratio has been observed in $MAPbBr_3$ SC.[36] Even if the type of doping can be reversed, intrinsic carrier densities of ~10^7 cm^{-3} for both p-type (Pb-poor) and n-type (Pb-rich) suggest a limited doping range achievable through precursors ratio variations.[32] Regarding now just extrinsic defect doping, impurities inclusion in $MAPbBr_3$ have also been studied with the particular objective to alter the unipolar p-type character described earlier.[33] Nevertheless, none of the impurities considered could achieve n-type doping, owing to heavy compensation from intrinsic defects, such as V_{Pb} and V_{Br}.[32,37] Based on these arguments and the lead deficient Pb/Br ratio measured by EDX, our $MAPbBr_3$ references could be effectively considered as p-doped material, where no benefits in terms of resistivity and electrical stability were obtained from adding Cl. We noticed that all attempts to measure the n- or p-type polarity of our $MAPbBr_3$ devices by hot probe method failed due to lack of reproducibility and stability of the results, most probably due to interference of parasitic ion migration during the measurements. It is worth noting that the way Cl^- anions interacts with the host crystal lattice is unknown. Considering that we are dealing with a solid solution, according to the XRD data, one considers that Cl substitutes Br in the octahedron. However, potentially other positions could be held by Cl^- anions, such as interstitials Cl_i, creating new defects as well as inducing other defects with other chemical species and/or band structure modifications. We have to take into consideration that adding Cl in solution impacts several aspects such as the chemistry involved while building the crystal in solution (change in solubility, diversity of lead complexes involved by addition of MACl). Incorporating Cl in the $MAPbBr_3$ structure would improve the resistivity and hysteresis like for previous work for given set of defects thanks to the interactions of Cl with these, causing the reported changes in electrical properties.

An important point should be made to partially explain the diversity of optoelectronic properties found in literature for $MAPbBr_3$, $MAPb(Br_{1-x}Cl_x)_3$ and $MAPbCl_3$, which can also be extended to all type of perovskites. The properties of a perovskite material depends intrinsically on the crystal growth and associated methods. In the literature, different synthesis techniques with different experimental settings are being employed sometimes to produce crystals that are then subsequently compared for a single characteristic or property. In the case of SCs, even for the Inverse Temperature Crystallization (ITC) method, sample-to-sample variability in crystal quality and performance is well known for $MAPbBr_3$, which can exceed an order of magnitude for a given optoelectronic property very easily.[32] Indeed, the crystal quality depends significantly on various experimental parameters such as thermodynamic equilibrium, impurity rate, supersaturation regime applied to the solution through rate and nature of the employed temperature ramp. Optimization of SC growth has been one of our main targets to attain device sampling reproducibility.[15,38] When comparing SCs grown by abrupt ITC method (heating up precursors solution till passing supersaturation limit temperature), linear temperature and adaptive temperature ramps (MITC methods) taking into consideration solution supersaturation evolution throughout crystal growth, one can reduce the variability in crystalline quality and optoelectronic properties for the latter. Nevertheless, even for crystals within an optimized crystal growth production batch can present elements pathologically bad or with above average performance despite having reduced this variability. We are then potentially discussing about apparent maxima/minima with non-optimized SCs that could be benefiting from Cl addition. This being said, small amounts of chloride could potentially have a positive impact on resistivity or sensitivity for SCs with certain type of defects where a dopant compensation mechanism could take place.

While the benefit of Cl incorporation on the electrical properties remained elusive, it could still boost the device performance for X-ray direct detection through indirect ways. We measured photocurrent pulses under X-ray illumination to acquire the sensitivity values for the different $MAPb(Br_{1-x}Cl_x)_3$ compositions under IEC 62220 International Standard conditions[39] and for RQA5 spectral quality: see Figure 3B-2 for average sensitivity S_{avg} values and Figure S18 as an example of stable photocurrent generated under pulsed X-rays irradiation for the $MAPb(Br_{0.85}Cl_{0.15})_3$ SC device. Comparable S_{avg} values were extracted by using a specific and reproducible biasing protocol that allow calculating the sensitivity in a standard gain-less Ramo regime (see Experimental Section and Supporting Information). An evident difference is seen once again between $MAPbBr_3$ and $MAPbCl_3$. The former shows an average sensitivity value of S_{avg} = 0.88 μC mGy_{air}^{-1} cm^{-2} and the latter an average value of S_{avg} = 0.40 μC mGy_{air}^{-1} cm^{-2}, both evaluated at +50 V mm^{-1}. For intermediate compositions $MAPb(Br_{1-x}Cl_x)_3$, an optimal performance was found for $MAPb(Br_{0.85}Cl_{0.15})_3$ reaching a sensitivity value of $S_{avg} = 1.87$ μC mGy_{air}^{-1} cm^{-2} in average and a maximal one of S ≈ 3 μC mGy_{air}^{-1} cm^{-2} at +50 V mm^{-1}. This value is higher than the sensitivity of CsI(Tl) - or a-Se-based flat panels (0.5 and 0.3 μC mGy_{air}^{-1} cm^{-2} at RQA5 spectral quality, respectively). Thus, $MAPb(Br_{0.85}Cl_{0.15})_3$ appears as the most promising composition in this study, doubling $MAPbBr_3$ sensitivity and coupled with the Pb/X ratio closest to stoichiometry. Such improvement in sensitivity may be related to a change in the charge collection efficiency symbolized by the μτ product.[40] This eventuality is discussed further down.

To get a better insight in the Cl effect on the optoelectronic properties, we measured the charge carrier mobility as a function of Cl content by using laser ToF technique. In contrast to resistivity and sensitivity, a decrease in hole mobility μ_h was observed when Cl content increases: see Figure 3B-3 for average hole values and Figure S15 for examples of transit times recorded during ToF measurements per composition. It is worth pointing out that no electron mobility μ_e could be satisfactorily drawn from the measurements. The reason for that has already been explained by our group in a previous work for $MAPbBr_3$ SC devices: the mobility-lifetime product of electrons ($\mu_e\tau_e$) is not large enough to allow electrons to fully transit their path.[11,41] Even though the average hole mobility $\mu_{h\text{-}avg}$ decreases from 15.8 to 9.2 cm² V^{-1} s^{-1} for $MAPbBr_3$ and $MAPb(Br_{0.85}Cl_{0.15})_3$, respectively, sensitivity doubles, meaning an enhancement of the $\mu_h\tau_h$ product, and therefore a potential increase in hole lifetime τ_h.

To explain such longer lifetime of charge carriers in $MAPb(Br_{1-x}Cl_x)_3$ materials, a few mechanisms highlighting band and defect structural alterations have been proposed. Firstly, Li et al.[28] reported, by using time-resolved photoluminescence spectroscopy with two-photon femtosecond laser excitation experiments, that incorporation of Cl inside SCs to a maximum of %Cl = 19 ($MAPb(Br_{0.81}Cl_{0.19})_3$) would create longer lifetime. Higher concentrations of Cl in the SC bulk would lead to measurable defect formation within the crystal, acting as trapping sites effectively reducing the PL lifetime. A Rashba effect in the bulk was theorized to be at the origin of this longer lifetime.[28] Secondly, another hypothesis presented by Tyler Mix et al.,[42] via transient reflectivity spectroscopy and nonadiabatic molecular dynamics simulations, explained that the addition of Cl increases the observed rate of hot carrier cooling and the calculated electron−phonon coupling constants, presenting a smaller ambipolar mobility,[42] which would be consistent with our hole mobility evolution. Incorporation of Cl^- anions would effectively induce more structural fluctuations in $MAPb(Br_{1-x}Cl_x)_3$ than in pristine samples, additionally causing excess energy to dissipate faster and subsequently stabilizing charge carriers.

Even if two-photon-excited photoluminescence, reflectivity and laser ToF measurements rely on different phenomena, the underlying physics should be the same and lifetime is expected to increase with increasing Cl content up to a certain limit, thanks to mechanisms such as the Rashba effect and/or faster hot carrier cooling. During ToF experiments, the electron transit time was not high enough to exceed the electron lifetime, hence no improvement nor degradation of it with varying Cl content could be evaluated. Despite this and not having measured μ_e, the same logic as for holes could be applied to electron: a gradual increase of lifetime τ_e could be considered while incorporating chloride in the $MAPbBr_3$ structure, thus leading to an improvement of the electron diffusion length.

To back up this hypothesis of longer lifetime for both charge carriers, modeling has been performed on S-V data to extract mobility-lifetime of the SC devices. Mobility-lifetime product estimation using Hecht equation (Equation S14)[43] or the so-called modified Hecht equation (Equation S15)[44–46] is a powerful tool to assess the quality of an X-ray sensitive semiconductor. It relies essentially on the measurement of the photocurrent – or time integral of the photocurrent – flowing in the material under X-ray illumination as a function of the externally applied bias. These equations must be handled with great care, as they are based on several assumptions that shall be verified beforehand. First, the commonly used Equations S14 and S15 derivate from the Ramo theorem and only describe the current induced on the electrodes by the motion of photogenerated charges inside a semiconductor in the presence of charge recombination via trapping sites.[47] Hence Equations S14 and S15 rule out any contribution that may originates from other effects that might alter the mobility-lifetime product values extracted from the Hecht fits, such as photoconductive gain.[48] Secondly, these equations assume the following starting hypotheses: i) the device has a planar geometry (the electrodes face each other and their dimensions largely exceed the thickness of the detector); ii) each charge carrier is defined by one mobility value that is constant with the electric field, the charge carrier can only be trapped once (no detrapping); and iii) the electric field E is uniform throughout the detector and is equal to V/L. It is critical that this last hypothesis (E = V/L) is verified in order to fit correctly the data using Hecht equation. Yet, a growing number of reports tend to point out that an externally applied bias displaces mobile ions toward the electrodes interfaces, and lead to distortion of the electric field in the device.[49–51] Ion accumulation at the vicinity of the electrode may occur more intensely during steady-state measurements involving continuous biasing procedures,[52] which is typically the case of X-ray induced photocurrent measurements. Such effects attributed to ion migration have been reported for several perovskite materials, $MAPbBr_3$,[49,53] $CsPbBr_3$[54] and $MAPbI_3$,[55] and thus seem to be a typical feature of perovskite optoelectronics. This must be taken into account when one carries out estimation of mobility-lifetime products, as a non-uniform electric field in the device may alter the quality of the Hecht fits and lead to wrong conclusions.[56]

That being said, we performed a complete analysis of the integrated currents generated under X-ray pulses with medical-grade beam quality, and fit the data using the two-carriers Hecht equation (Equation 1) to extract both electron and holes mobility-lifetime products:[57]

$$\eta(x,V) = \frac{\mu_e \tau_e V}{L^2}\left[1 - e^{-\frac{xL}{\mu_e \tau_e V}}\right] + \frac{\mu_h \tau_h V}{L^2}\left[1 - e^{-\frac{L(L-x)}{\mu_h \tau_h V}}\right] \#(1)$$

Where η is the charge induction efficiency; μ_e and μ_h are the mobilities of electrons and holes (cm^2 V^{-1} s^{-1}), respectively; $\tau_e$and τ_h are the lifetimes of electrons and holes (s), respectively; L is the device thickness (cm); x is the X-ray interaction position in the crystal (cm); V is the applied bias (V). Unlike the one-carrier Hecht equation, the two-carriers counterpart considers the contribution of both electron and holes to the photocurrent, and thus requires to take into account the distribution of photogenerated charges that decays exponentially within the depth of the material (see Figures 4A and S19). Both, this distribution and the electron-hole pair reaction energy were adapted for each crystal composition. This leads to a more accurate evaluation of mobility-lifetime products for high X-ray energies, as well as discrimination of electron and holes mobility-lifetime products. In Figure 4A, the electrons and holes flow in the negative and positive x direction, with $\mu_e \tau_e V/L$ and $\mu_h \tau_h V/L$ being the mean free path of electrons and holes, respectively, while X-rays enter the device at the anode. It should be noted that we considered a uniform electric field in our model. The relevancy of this assumption depending on the sample composition will be discussed later on. For more details, see Supporting Information. A deeper work is underway considering a non-uniform electric field as well as several types of trapping centers, which will be published in a future paper.

The model depicted above was used to fit the experimental sensitivities under X-rays for each perovskite sample (see Experimental Section). All the S-V curves and the best corresponding fits are plotted in Figure S21, S values are normalized by the maximal theoretical values S_{max} (defined by Equation S19).

On the one hand, it can be seen that for most of the samples, the experimental data fit poorly to the model. More precisely, for all $MAPbBr_3$, $MAPb(Br_{0.98}Cl_{0.02})_3$ $MAPb(Br_{0.97}Cl_{0.03})_3$ samples and almost all $MAPb(Br_{0.92}Cl_{0.08})_3$ samples, the S-V curves reach a plateau with increasing voltage with a lower value than that of the model prediction. This essentially means that even with bias values extending to infinity the charge induction efficiency will never reach unity – which is not in accordance with Equation 1. Figure 4B depicts an example of generated photocurrent in $MAPbBr_3$ SC device under X-ray irradiation at three different voltages and Figure 4D shows its associated experimental data and Hecht modeling. An explanation lies in the relevancy of the starting hypothesis: E = V/L, which is implicitly or explicitly admitted in the vast majority of publications involving perovskite ionizing radiation detectors.[2,44,45,58–61] Yet a non-constant electric field in the device will greatly change the outcome of the Hecht fits, as it has been showed in previous works for linear decreasing electric fields.[49,56] In addition, Liu et al. showed that ion accumulation at the vicinity of the electrodes leads to significant decrease of the electric field in the volume of the detector as the net charges induce by the mobile ions screen the externally applied electric field.[51] This effect creates in the middle of the detector a “dead zone” for the photogenerated charges, severely impeding the charge induction efficiency.

On the other hand, the model fits correctly for at least one $MAPb(Br_{0.92}Cl_{0.08})_3$ and two $MAPb(Br_{0.85}Cl_{0.15})_3$ crystals, which implies that there is uniformity of the electric field in all the volume of the detector for these samples. Figure 4C depicts an example of generated photocurrent in $MAPb(Br_{0.85}Cl_{0.15})_3$ SC device under X-ray irradiation at three different voltages and Figure 4E shows its associated experimental data and Hecht modeling. We believe this improvement of the fit stems from the increase of the Pb/X ratio which gets closer to the ABX_3 stoichiometry with increasing Cl content (Figure 1B). Being closer to stoichiometry translates into a reduction of the density of defects (e.g. halide vacancies V_X) that in halide perovskites are mobile and contribute to ions mobility upon application of an external electric field.[29,55,62] Also, at a local level, while Br^- anions would screen each other (low binding energy with Pb), Cl^- anions would reduce this screening in the inorganic octahedrons resulting in ion migration, probably due to difference in binding between Pb-Cl and Pb-Br.[22] The lower defect density in $MAPb(Br_{0.92}Cl_{0.08})_3$ and $MAPb(Br_{0.85}Cl_{0.15})_3$ crystals would prevent the build-up of the ionic space charges near the electrodes, and maintain the uniformity of the electric field in the device. These results are in good accordance with the observed decrease in conductivity drift with increasing Cl content (Table S4). Conductivity drift is widely attributed to the movement of mobile ions, and it was reported that lower density of defects associated to mobile ions reduces dark current drift.[63,64] More specifically for series 4 $MAPb(Br_{0.85}Cl_{0.15})_3$ SC device, the two-carriers Hecht model fits the experimental data well and yields very high mobility-lifetime product value of $\mu_h\tau_h = 8 \times 10^{-4}$ cm² V⁻¹ for holes and $\mu_e\tau_e = 3 \times 10^{-4}$ cm² V⁻¹ for electrons, respectively. By using laser ToF-determined hole mobility μ_h, hole lifetime for $MAPbBr_3$ and $MAPb(Br_{0.85}Cl_{0.15})_3$ are estimated at $\tau_h = 7$ µs and $\tau_h = 75$ µs, respectively, confirming to some extent our initial hypothesis. These values are in accordance with the hole ToF measurements themselves. Figure S16 shows the ToF hole current waveforms for $MAPbBr_3$ and $MAPb(Br_{0.85}Cl_{0.15})$ devices at different biases. For $MAPb(Br_{0.85}Cl_{0.15})$, a clear inflection of the waveform can be observed at a moderate voltage of 50V, indicating a transit time for holes of $t_t = 2$ µs. It implies that the lifetime of holes cannot be lower than 2 µs in the drift-diffusion regime. These lifetimes in the microsecond range agree with results from previous works.[49,65] All $\mu\tau$ product values for both electrons and holes extracted from two-charge carriers Hecht model are displayed in Table S5. These values are significantly better than that of a-Se, comparable to that of highest quality TlBr and close to that of the state of the art materials for high-energy radiation detection CdTe and CZT (see Table 1).[66–69] However these results suggest that further development in the base material quality and/or synthesis is needed to attain state-of-the-art performances (e.g. precursors purification, doping, post-treatments).

Additionally and as complement to the discussion, dark current density $J_{dark\text{-}avg}$ values were also extracted (Figure S17) and remained unchanged with increasing Cl content for mixed halide compositions when compared to base material. Nevertheless, Figure 5 illustrates the benefits of doping $MAPbBr_3$ with $\%Cl_{cryst} = 15$ ($MAPb(Br_{0.85}Cl_{0.15})_3$) in chloride for this study. Sensitivity values were normalized per sample by the X-ray absorbed fraction (% absorbed X-ray), calculated using Equation S20, to take into account the dimensions of resulting SC devices, specially their different thicknesses (see Figure S3 and Table S6 for more information). $MAPb(Br_{0.85}Cl_{0.15})_3$ stands out as the most interesting composition for detection of medical-grade X-rays of this study by showing the highest S values ($S_{avg} = 1.87$ µC mGy_{air}^{-1} cm^{-2} at 50 V mm^{-1}) and the lowest J_{dark} values recorded ($J_{dark\text{-}avg} = 43.4$ nA mm^{-2} at 50 V mm^{-1}).

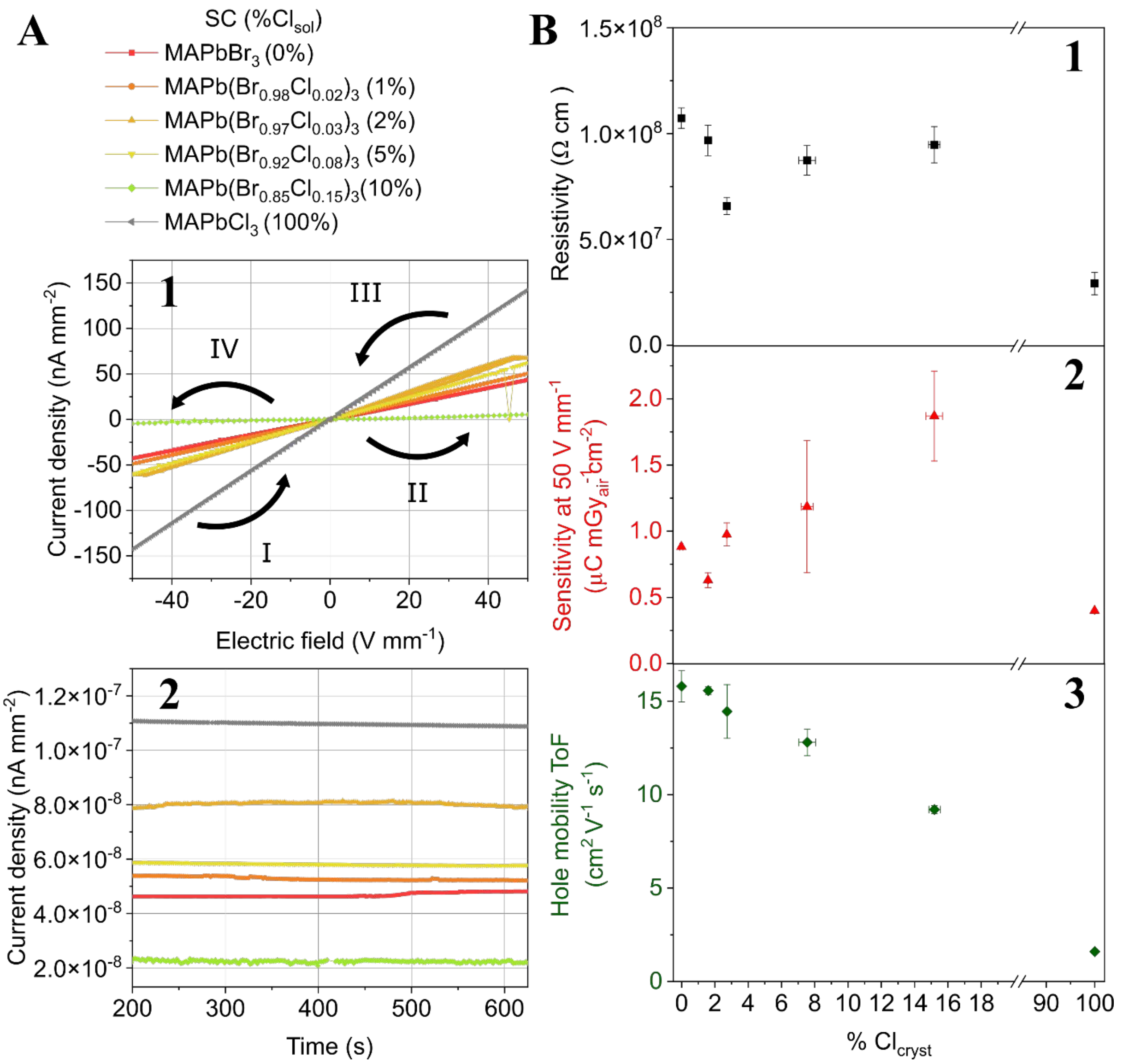

Figure 3. Optoelectronic performance of MAPb(Br$_{1-x}$Cl$_x$)$_3$ SC devices. (A)(1) Example of J-V sweeps performed for a series of MAPb(Br$_{1-x}$Cl$_x$)$_3$ SCs forward from -50 V mm^{-1} to +50 V mm^{-1} (step I then II) and reverse from +50 V to -50 V (step III then IV). **(2)** Dark current stability of MAPb(Br$_{1-x}$Cl$_x$)$_3$ SC devices under electrical field of 50 V mm^{-1}. **(B)** MAPb(Br$_{1-x}$Cl$_x$)$_3$ SCs resulting average **(1)** resistivity ρ, **(2)** sensitivity S and **(3)** hole mobility μ_h measurements as a function of crystal Cl content %Cl$_{cryst}$. Resistivity is left unchanged by Cl addition, while sensitivity doubles for MAPb(Br$_{0.85}$Cl$_{0.15}$)$_3$ and hole mobility decreases steadily with increasing Cl content.

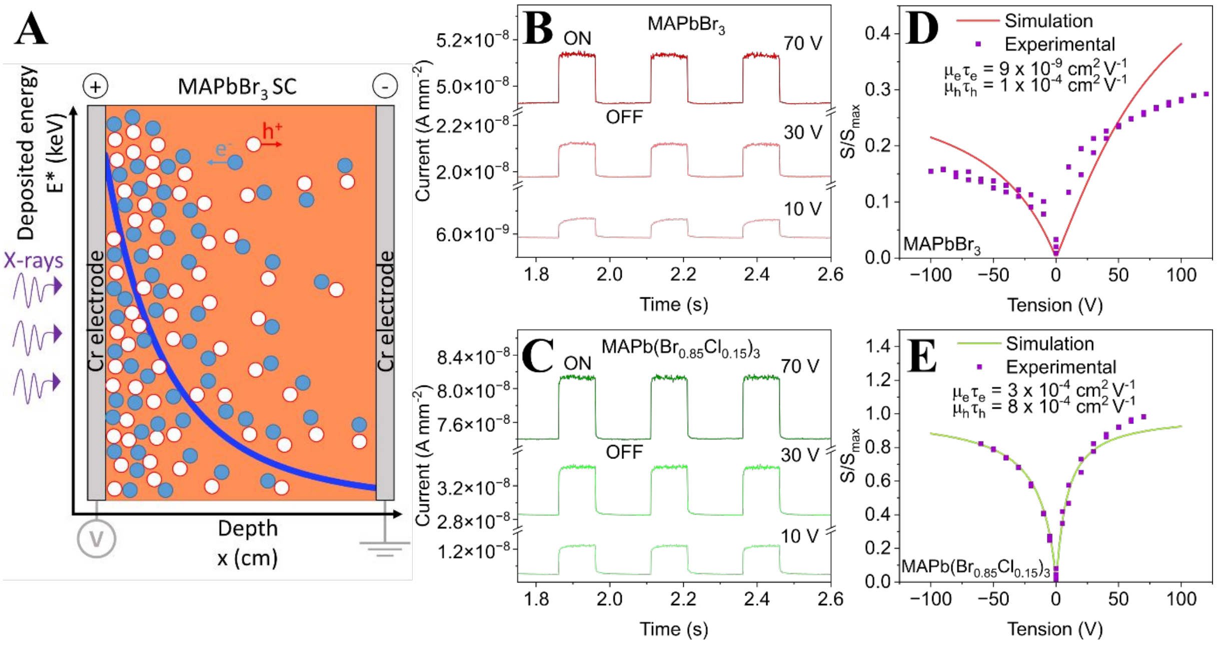

Figure 4. Two-charge carriers Hecht modelling. (A) Schematic representation of photogenerated charge carriers in MAPbBr$_3$ SC device with Cr electrodes while being under X-ray illumination at the anode and under bias. The deposited energy *E** is plotted as a function of the X-ray interaction position in the crystal bulk (blue line). Photocurrent generated under pulsed X-ray irradiation during 100 ms at 4 Hz on **(B)** MAPbBr$_3$ and **(C)** MAPb(Br$_{0.85}$Cl$_{0.15}$)$_3$ SC devices for sensitivity measurements at 10, 30 and 70 V. **(D)** Series 1 MAPbBr$_3$ SC device S-V simulation (red plot) and experimental (purple plot) curves and **(E)** series 4 MAPb(Br$_{0.85}$Cl$_{0.15}$)$_3$ SC device S-V simulation (green plot) and experimental (purple plot) curves. The simulated S-V curve results from the Hecht fit for two-charge carriers. Associated μτ products are displayed in inset.

Table 1. $MAPbBr_3$, $MAPb(Br_{0.85}Cl_{0.15})_3$ and some known ionizing radiation detectors, mobility μ, lifetime τ and $\mu\tau$ product values for electrons and holes

Material	Electron mobility μ_e [$cm^2\ V^{-1}\ s^{-1}$]	Hole mobility μ_h [$cm^2\ V^{-1}\ s^{-1}$]	Electron lifetime τ_e [s]	Hole lifetime τ_h [s]	$\mu_e\tau_e$ product [$cm^2\ V^{-1}$]	$\mu_h\tau_h$ product [$cm^2\ V^{-1}$]
a-Se[a]	0.005	0.14	10^{-6}	10^{-6}	5×10^{-9}	1.4×10^{-7}
TlBr[a]	6	-	2.5×10^{-6}	-	1.6×10^{-5}	1.5×10^{-6}
CdTe[a]	1100	100[6]	3×10^{-6}	2×10^{-6}	3.3×10^{-3}	2×10^{-4}
CdZnTe (CZT)[a]	1350	120	10^{-6}	5×10^{-8}	1×10^{-3}	6×10^{-6}
$MAPbBr_3$[b]	-	15[c]	-	7×10^{-6}[d]	9×10^{-7}	1×10^{-4}
$MAPb(Br_{0.85}Cl_{0.15})_3$[b]	-	11[c]	-	7.5×10^{-5}[d]	2.5×10^{-4}	8×10^{-4}

[a] Extracted from reference[66];

[b] This work: series 3 $MAPbBr_3$ and series 4 $MAPb(Br_{0.85}Cl_{0.15})_3$ were chosen here for the comparative table because of their relatively good Hecht fitting for two-charge carriers;

[c] Hole mobilities μ_h determined via laser ToF measurements;

[d] Hole lifetime τ_h were estimated from two-charge carriers Hecht fitting $\mu_h\tau_h$ for holes and the measured laser ToF hole mobility μ_h;

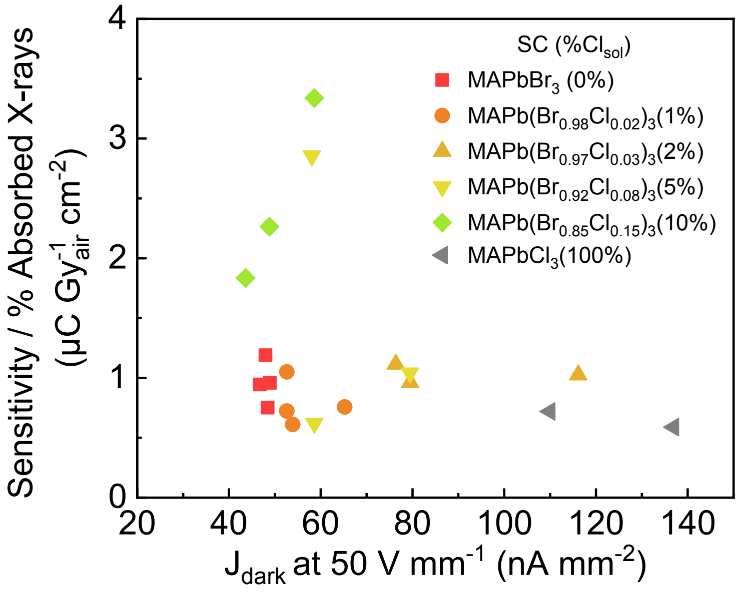

Figure 5. Sensitivity normalized by the percentage of absorbed X-rays as a function of dark current density J_{dark} at 50 V mm^{-1}. $MAPb(Br_{0.85}Cl_{0.15})_3$ stands out as the most interesting material thanks to its low dark current density and the highest sensitivity of this work.

3. CONCLUSIONS

This study presents evidence of the successful substitution of Br^- by Cl^- anions in $MAPbBr_3$ SCs, with a careful quantification of the crystal bulk Cl content. The results partially corroborate previous works on this material.[2,19,20] Optoelectronic evaluation, meticulously performed in X-ray medical radiography conditions and backed up by a systematic crystal batch production and coupled with other characterization techniques, reveals the high quality of synthesized $MAPb(Br_{1-x}Cl_x)_3$ SCs, exhibiting no hysteresis during current-voltage measurements and negligible conductivity drift. This linked to the optimized–growth nature of $MAPb(Br_{1-x}Cl_x)_3$ SCs produced by our method, with few and reproducible defect structures. We present here an optimum in Cl content for $MAPb(Br_{0.85}Cl_{0.15})_3$, standing out as the most interesting composition by showing the highest sensitivity ($S \approx 3$ μC mGy$_{air}^{-1}$ cm^{-2} at 50 V mm^{-1}), the lowest dark current density ($J_{dark} \approx 22$ nA mm^{-2} at 50 V mm^{-1}) and the lowest conductivity drift ($\sigma_{drift} \approx 3$ S m^{-1} s^{-1} at 50 V mm^{-1}). An extensive analysis of the X-ray induced photocurrent by a two-charge carriers Hecht model indicates superior charge transport properties in the $MAPb(Br_{0.85}Cl_{0.15})_3$ SC for both carrier types. Notably, EDX data suggest that Cl incorporation in the crystal lattice increases the Pb/X (X = Br, Cl) ratio that approaches ABX_3 stoichiometry for the $MAPb(Br_{0.85}Cl_{0.15})_3$ composition. We propose that this improvement in stoichiometry corresponds to a reduction of point defects in the lead-halide framework, thus to a lower fraction of mobile ionic defects (V_X, X_i), resulting in an enhancement of the charge induction efficiency under X-rays irradiation. In addition, while laser ToF measurements indicate that hole mobility decreases with increasing Cl content, the two-charge carriers Hecht model suggests that Cl incorporation increases the hole lifetime reaching $\tau_h = 75$ µs for $MAPb(Br_{0.85}Cl_{0.15})_3$. These results confirm the general good charge transport properties of $MAPb(Br_{1-x}Cl_x)_3$ perovskites, but underline that further effort needs to be done to reach state-of-the-art materials CdTe and CZT performances. We believe that our work could encourage better approaches to improve anion engineering with halide elements, crystal growth and associated high-energy radiation detection with hybrid halide perovskites.

4. EXPERIMENTAL SECTION

Materials. N,N-Dimethylformamide (DMF, Sigma-Aldrich, anhydrous, 99.8 %), Dimethyl sulfoxide (DMSO, Sigma-Aldrich, anhydrous, ≥ 99.9 %), $PbBr_2$ (Sigma-Aldrich, anhydrous 99.999 %), $PbCl_2$ (Sigma-Aldrich, 99.999 %), MABr (GreatCell Solar, ≥99 %), MACl (GreatCell Solar, ≥99 %), and Chromium metal (Sigma-Aldrich, powder, 99.5%, −100 mesh). The materials used for the preparation of the growth solution were used as-received.

MAPb(Br$_{1-x}$Cl$_x$)$_3$ SCs growth & device fabrication. Cl-containing SCs were grown via MITC method. The amount of chloride in solution %Cl$_{sol}$ was determined via Equations S1 to S3 in Supporting Information. The growth process was similar to the one described in previous work for MAPbBr$_3$.[15] The selected Cl contents in solution were %Cl$_{sol}$ = 0, 1, 2, 5, 10 and 100. For all samples, a stoichiometric amount of precursors was used PbX$_2$:MAX 1:1. For MAPbBr$_3$ and all mixed halide compositions, the amount of precursors was dissolved in DMF to obtain 1 M solutions. For MAPbCl$_3$, a 2 M solution was prepared by dissolving the precursors in a DMF/DMSO mixture (3:7 in volume).[27] Regarding the mixed halide compositions, the targeted %Cl$_{sol}$ was obtained by replacing part of MABr with MACl (check Table S1 for details). Different temperature ramps were employed to adapt the changes in solubility due to the different concentrations of Cl-species introduced. On the one hand, an average increase of 5.5°C h^{-1} for MAPbBr$_3$ (%Cl$_{sol}$ = 0) and %Cl$_{sol}$ = 1 and, on the other hand, an average increase of 1°C h^{-1} for %Cl$_{sol}$ = 2, 5 and 10 were used. While MAPbCl$_3$ (%Cl$_{sol}$ = 100), being grown in a completely different solvent (DMF:DMSO), its temperature ramp was also adjusted accordingly to 1.6°C h^{-1} as average increase. For each selected %Cl$_{sol,}$ firstly, a high quality seed of matching composition was obtained by spontaneous nucleation; secondly, a seed-assisted crystal growth took place to obtain the resulting SCs. At the end of the growth process, SCs of 4 mm × 4 mm × 2 mm on average and different crystal Cl content (%Cl$_{cryst}$) were obtained. They were mechanically polished to mirror grade quality and Cr electrodes were thermally evaporated on opposite sides. The Cr evaporation was performed by batches, each batch (series) consisting of a complete set of all six compositions. For more information, see Supporting Information.

UV-Visible spectroscopy & Tauc plot. For transmittance data, a Perkin Elmer Lambda 900 UV-Vis-NIR spectrometer was used with a wavelength range of 400-600 nm, a 0.1 nm step and equipped with a Tungsten lamp. Tauc plots were charted (Figure S9), using Equations S8 to S11, to extract the SCs respective optical bang gaps E_g. For more information, see Supporting Information.

PL. Spectra were recorded at room temperature with a double grating excitation and emission spectrometers Fluorolog-3 model FL3-22 and Horiba Jobin Yvon-Spex coupled to a R928 Hamamatsu photomultiplier. The excitation source was a Xe arc-lamp (450 W). A 350 nm excitation wavelength was used.

FESEM-EDX. To determine Cl content and Pb/X ratio of the SCs, a FESEM ZEISS Ultra+ associated with an EDX detector (©Bruker-SDD) working in high vacuum mode with a 10kV voltage and a beam diameter of 30 µm was used. For all measurement, the acquisition was fixed at 100 000 counts with a working distance of 8 mm. For data analysis, Stratagem ©SAMx software with P/B-ZAF mode for elemental quantification was used. The species taken into account were Cl, Br and Pb for quantification. The Cl content and Pb/X ratio were determined using Cl K_α, Br L_α and Pb M_α emission lines and Equations S5 and S6. The spectra were normalized by $MAPbBr_3$ Br L_α peak.

XRD. A D8 Endeavor diffractometer equipped with a Johanssonn monochromator working in Bragg-Brentano θ-2θ geometry was used (Cu Kα $\lambda = 1.5406$ Å). An acquisition time of 2.5 s was set using 0.01 ° step, 2θ values ranging from 5 ° to 90 °. Le Bail refinements using free software FullProf were performed for lattice parameters determination on diffractograms. Reliability factors for points with Bragg contributions are shown in Table S2.

J-V, J-t & sensitivity tests. The devices were measured in both dark and under X-ray irradiation conditions. The J-V characteristic was measured in the dark for electric fields ranging from -50 to +50 V mm^{-1} and using a 1 V s^{-1} scan rate. Each device was measured 5 times consecutively. Resistivity values were estimated from the linearization of the J-V curves. For J-t measurements, the samples were constantly biased at 50 V mm^{-1} and both dark current density and conductivity drift values were measured. Experimental sensitivity values were measured by irradiating the devices with ten X-ray pulses of 100 ms at 4 Hz, corresponding to 24 μGy$_{air}$ dose per pulse with a RQA5 spectrum (sealed tube with a W anode, 70 kV accelerating voltage, 23.5 mm total Al filtration) (see Figure 20). The incident X-ray dose was calibrated using a PTW Unidos dosimeter. The integration of the photocurrent over the pulse duration yields the measured charge Q. In order to reduce experimental errors, each photocurrent measurement was repeated and the measured charge Q averaged over 10 pulses and divided by the samples electrode surface area and dose yielding the sensitivity expressed in μC mGy$_{air}^{-1}$ cm^{-2}. By sweeping the externally applied bias, one can obtain the measured charge as function of bias, or in other words, the sensitivity-voltage (S-V) curve of the detector. These experimental data were fitted to Equation S18 by adjusting only two fitting parameters, namely mobility-lifetime product of electrons $\mu_e\tau_e$ and that corresponding to holes $\mu_h\tau_h$. The reader should take note that Equation S18 essentially consists of considering Equation S14 (one-carrier Hecht equation) for both charge carriers, and fixing the Q_0 value instead of leaving it as a free parameter. We believe that this prevents misinterpretation of S-V data. The experimental settings follow the characteristic medical radiography setups described in IEC 62220 International Standard.[39] All the sensitivity values provided in this work were evaluated at an electric field of 50 V mm^{-1}. The samples were tested right after Cr electrodes evaporation and exposed to the same radiation dose to have similar potential device damage under X-rays.[43] See Table S7, Figures S22 and S23 for further technical details. The size disparity of the SC devices results in different deposited Cr electrodes surface, illuminated surfaces and different X-ray absorbed fraction. This was taken into consideration by calculating for each SC device the sensitivity S normalized by the absorbed X-ray fraction (% absorbed X-ray) as of Beer-Lambert law. More details about mobility-lifetime product estimation using Hecht equation and calculation of the absorbed X-ray fraction are provided in Supporting Information.

ToF. A pulsed N_2 laser was employed using a 337 nm wavelength and a 800 ps impulsion time. The laser beam is attenuated by an optical filter with a transmission coefficient of 0.16 before irradiating semi-transparent 30 nm-thick chromium electrode of Cr/$MAPbBr_3$/Cr testing device. Charge carrier mobility was calculated using Equation S13. For more information about experimental setup see previous work and associated Supporting Information.[11]

ASSOCIATED CONTENT

Supporting Information.

Crystal growth details including photographs of experimental setup, solubility curves for $MAPbBr_3$ and $MAPb(Br_{0.85}Cl_{0.15})_3$ in DMF and crystal Cl contents and Pb/X ratios summary table; device fabrication details; overall EDX spectra and profile study data; overall XRD diffractograms, Vegard’s law, peak shift for (100) plane and Le Bail refinement data; ICP-MS data; Tauc plots data; PL spectra; J-V sweeps; dark current and conductivity drift data; photocurrent under X-rays measurement for $MAPb(Br_{0.85}Cl_{0.15})_3$; laser ToF measurement examples; average dark current densities per composition at 50 V mm^{-1}; mobility-lifetime product estimation using Hecht equation, S-V data and associated modeling; X-ray absorbed fraction determination; settings details including photographs of medical experimental setup.

AUTHOR INFORMATION

Corresponding Authors

Javier Mayén Guillén – Grenoble Alpes University, CEA, LITEN, DTNM, F38000 Grenoble, France

Ferdinand Lédée - Grenoble Alpes University, CEA, LETI, DOPT, F38000 Grenoble, France

Authors

Oriane Baussens - Grenoble Alpes University, CEA, LETI, DOPT, F38000 Grenoble, France

Marian Chapran - Grenoble Alpes University, CEA, LETI, DOPT, F38000 Grenoble, France

Thibault Lemercier - Grenoble Alpes University, CNRS, Grenoble INP, Institut Néel, F38042 Grenoble, France

Jean-Marie Verilhac – Grenoble Alpes University, CEA, LITEN, DTNM, F38000 Grenoble, France

Eric Gros Daillon – Grenoble Alpes University, CEA, LETI, DOPT, F38000 Grenoble, France

Alain Ibanez - Grenoble Alpes University, CNRS, Grenoble INP, Institut Néel, F38042 Grenoble, France

Julien Zaccaro - Grenoble Alpes University, CNRS, Grenoble INP, Institut Néel, F38042

Grenoble, France

Authors Contributions

The manuscript was written through contributions of all authors. All authors have given approval to the final version of the manuscript.

Funding Sources

European Union’s Horizon 2020 research and innovation program.

Notes

The authors declare no conflict of interest.

ACKNOWLEDGMENTS

The authors wish to thank Sebastien Pairis for his assistance in collecting the EDX spectra and their interpretation. This work has received funding from the European Union’s Horizon 2020 research and innovation program under the Photonics Public Private Partnership (www.photonics21.org) with the project PEROXIS under Grant Agreement No. 871336. ICP-MS equipment is part of the NanoID platform that was supported by the French Investissements d’Avenir ANR-10-EQPX-39.

REFERENCES

(1) Johns, P. M.; Baciak, J. E.; Nino, J. C. Enhanced Gamma Ray Sensitivity in Bismuth Triiodide Sensors through Volumetric Defect Control. *Appl. Phys. Lett.* **2016**, *109* (9), 092105. https://doi.org/10.1063/1.4962293.

(2) Wei, H.; DeSantis, D.; Wei, W.; Deng, Y.; Guo, D.; Savenije, T. J.; Cao, L.; Huang, J. Dopant Compensation in Alloyed CH3NH3PbBr3−xClx Perovskite Single Crystals for Gamma-Ray Spectroscopy. *Nature Mater* **2017**, *16* (8), 826–833. https://doi.org/10.1038/nmat4927.

(3) Wei, H.; Fang, Y.; Mulligan, P.; Chuirazzi, W.; Fang, H.-H.; Wang, C.; Ecker, B. R.; Gao, Y.; Loi, M. A.; Cao, L.; Huang, J. Sensitive X-Ray Detectors Made of Methylammonium Lead Tribromide Perovskite Single Crystals. *Nature Photon* **2016**, *10* (5), 333–339. https://doi.org/10.1038/nphoton.2016.41.

(4) Tisdale, J. T.; Yoho, M.; Tsai, H.; Shrestha, S.; Fernando, K.; Baldwin, J. K.; Tretiak, S.; Vo, D.; Nie, W. Methylammonium Lead Tribromide Single Crystal Detectors towards Robust Gamma-Ray Photon Sensing. *Adv. Optical Mater.* **2020**, 2000233. https://doi.org/10.1002/adom.202000233.

(5) Liu, Y.; Zhang, Y.; Zhu, X.; Feng, J.; Spanopoulos, I.; Ke, W.; He, Y.; Ren, X.; Yang, Z.; Xiao, F.; Zhao, K.; Kanatzidis, M.; Liu, S. (Frank). Triple-Cation and Mixed-Halide Perovskite Single Crystal for High-Performance X-ray Imaging. *Adv. Mater.* **2021**, *33* (8), 2006010. https://doi.org/10.1002/adma.202006010.

(6) Dong, Q.; Fang, Y.; Shao, Y.; Mulligan, P.; Qiu, J.; Cao, L.; Huang, J. Electron-Hole Diffusion Lengths > 175 Mm in Solution-Grown CH $_3$ NH $_3$ PbI $_3$ Single Crystals. *Science* **2015**, *347* (6225), 967–970. https://doi.org/10.1126/science.aaa5760.

(7) Yin, W.-J.; Shi, T.; Yan, Y. Unusual Defect Physics in CH $_3$ NH $_3$ PbI $_3$ Perovskite Solar Cell Absorber. *Appl. Phys. Lett.* **2014**, *104* (6), 063903. https://doi.org/10.1063/1.4864778.

(8) Basiricò, L.; Ciavatti, A.; Fraboni, B. Solution-Grown Organic and Perovskite X-Ray Detectors: A New Paradigm for the Direct Detection of Ionizing Radiation. *Adv. Mater. Technol.* **2021**, *6* (1), 2000475. https://doi.org/10.1002/admt.202000475.

(9) Saidaminov, M. I.; Abdelhady, A. L.; Murali, B.; Alarousu, E.; Burlakov, V. M.; Peng, W.; Dursun, I.; Wang, L.; He, Y.; Maculan, G.; Goriely, A.; Wu, T.; Mohammed, O. F.; Bakr, O. M. High-Quality Bulk Hybrid Perovskite Single Crystals within Minutes by Inverse Temperature Crystallization. *Nat Commun* **2015**, *6* (1), 7586. https://doi.org/10.1038/ncomms8586.

(10) Saidaminov, M. I.; Abdelhady, A. L.; Maculan, G.; Bakr, O. M. Retrograde Solubility of Formamidinium and Methylammonium Lead Halide Perovskites Enabling Rapid Single Crystal Growth. *Chem. Commun.* **2015**, *51* (100), 17658–17661. https://doi.org/10.1039/C5CC06916E.

(11) Baussens, O.; Maturana, L.; Amari, S.; Zaccaro, J.; Verilhac, J.-M.; Hirsch, L.; Gros-Daillon, E. An Insight into the Charge Carriers Transport Properties and Electric Field Distribution of CH $_3$ NH $_3$ PbBr $_3$ Thick Single Crystals. *Appl. Phys. Lett.* **2020**, *117* (4), 041904. https://doi.org/10.1063/5.0011713.

(12) Arya, S.; Mahajan, P.; Gupta, R.; Srivastava, R.; Tailor, N. kumar; Satapathi, S.; Sumathi, R. R.; Datt, R.; Gupta, V. A Comprehensive Review on Synthesis and Applications of Single Crystal Perovskite Halides. *Progress in Solid State Chemistry* **2020**, 100286. https://doi.org/10.1016/j.progsolidstchem.2020.100286.

(13) Feng, A.; Xie, S.; Fu, X.; Chen, Z.; Zhu, W. Inch-Sized Thin Metal Halide Perovskite Single-Crystal Wafers for Sensitive X-Ray Detection. *Front. Chem.* **2022**, *9*, 823868. https://doi.org/10.3389/fchem.2021.823868.

(14) Juarez-Perez, E. J.; Hawash, Z.; Raga, S. R.; Ono, L. K.; Qi, Y. Thermal Degradation of $CH_3NH_3PbI_3$ Perovskite into NH_3 and CH_3I Gases Observed by Coupled Thermogravimetry–Mass Spectrometry Analysis. *Energy Environ. Sci.* **2016**, *9* (11), 3406–3410. https://doi.org/10.1039/C6EE02016J.

(15) Amari, S.; Verilhac, J.-M.; Gros D'Aillon, E.; Ibanez, A.; Zaccaro, J. Optimization of the Growth Conditions for High Quality $CH_3NH_3PbBr_3$ Hybrid Perovskite Single Crystals. *Crystal Growth & Design* **2020**, *20* (3), 1665–1672. https://doi.org/10.1021/acs.cgd.9b01429.

(16) Kasap, S. O.; Rowlands, J. A. Direct-Conversion Flat-Panel X-Ray Image Detectors. *IEE Proceedings - Circuits, Devices and Systems* **2002**, *149* (2), 85–96. https://doi.org/10.1049/ip-cds:20020350.

(17) Datta, A.; Zhong, Z.; Motakef, S. A New Generation of Direct X-Ray Detectors for Medical and Synchrotron Imaging Applications. *Sci Rep* **2020**, *10* (1), 20097. https://doi.org/10.1038/s41598-020-76647-5.

(18) He, Y.; Matei, L.; Jung, H. J.; McCall, K. M.; Chen, M.; Stoumpos, C. C.; Liu, Z.; Peters, J. A.; Chung, D. Y.; Wessels, B. W.; Wasielewski, M. R.; Dravid, V. P.; Burger, A.; Kanatzidis, M. G. High Spectral Resolution of Gamma-Rays at Room Temperature by Perovskite CsPbBr3 Single Crystals. *Nat Commun* **2018**, *9* (1), 1609. https://doi.org/10.1038/s41467-018-04073-3.

(19) Rybin, N.; Ghosh, D.; Tisdale, J.; Shrestha, S.; Yoho, M.; Vo, D.; Even, J.; Katan, C.; Nie, W.; Neukirch, A. J.; Tretiak, S. Effects of Chlorine Mixing on Optoelectronics, Ion Migration, and Gamma-Ray Detection in Bromide Perovskites. *Chem. Mater.* **2020**, *32* (5), 1854–1863. https://doi.org/10.1021/acs.chemmater.9b04244.

(20) Qiu, L.; Wang, Z.; Luo, S.; Li, C.; Wang, L.; Ke, S.; Shu, L. Perovskite MAPb(Br1−Cl)3 Single Crystals: Solution Growth and Electrical Properties. *Journal of Crystal Growth* **2020**, *549*, 125869. https://doi.org/10.1016/j.jcrysgro.2020.125869.

(21) Mannodi-Kanakkithodi, A.; Park, J.-S.; Martinson, A. B. F.; Chan, M. K. Y. Defect Energetics in Pseudo-Cubic Mixed Halide Lead Perovskites from First-Principles. *J. Phys. Chem. C* **2020**, *124* (31), 16729–16738. https://doi.org/10.1021/acs.jpcc.0c02486.

(22) Wang, X.; Li, Y.; Xu, Y.; Pan, Y.; Wu, Y.; Li, G.; Huang, Q.; Zhang, Q.; Li, Q.; Zhang, X.; Chen, J.; Lei, W. Ion Migrations in Lead Halide Perovskite Single Crystals with Different Halide Components. *Phys. Status Solidi B* **2020**, 1900784. https://doi.org/10.1002/pssb.201900784.

(23) Jena, A. K.; Kulkarni, A.; Miyasaka, T. Halide Perovskite Photovoltaics: Background, Status, and Future Prospects. *Chem. Rev.* **2019**, *119* (5), 3036–3103. https://doi.org/10.1021/acs.chemrev.8b00539.

(24) Jiang, W.; Di, H.; Sun, H.; Zhao, C.; Liao, F.; Zhao, Y. Role of DMSO Concentration in the Crystallization Process of MAPbBr3 Perovskite Single Crystal Films. *Journal of Crystal Growth* **2020**, *550*, 125880. https://doi.org/10.1016/j.jcrysgro.2020.125880.

(25) Liu, F.; Yoho, M.; Tsai, H.; Fernando, K.; Tisdale, J.; Shrestha, S.; Baldwin, J. K.; Mohite, A. D.; Tretiak, S.; Vo, D. T.; Nie, W. The Working Principle of Hybrid Perovskite Gamma-Ray Photon Counter. *Materials Today* **2020**, S1369702120300730. https://doi.org/10.1016/j.mattod.2020.02.022.

(26) Jiang, S.; Wang, X.; Wu, Y.; Li, Y.; Zhang, Q.; Li, G.; Wu, Y.; Zhang, W.; Zhang, X.; Wang, B.; Chen, J.; Lei, W. Balance Lead in Solution-Processed CH3NH3PbBrxCl(3−x)

Single Crystals for High Performance X-Ray Detection. *Materials Letters* **2019**, *236*, 26–29. https://doi.org/10.1016/j.matlet.2018.10.055.

(27) Maculan, G.; Sheikh, A. D.; Abdelhady, A. L.; Saidaminov, M. I.; Haque, M. A.; Murali, B.; Alarousu, E.; Mohammed, O. F.; Wu, T.; Bakr, O. M. $CH_3NH_3PbCl_3$ Single Crystals: Inverse Temperature Crystallization and Visible-Blind UV-Photodetector. *J. Phys. Chem. Lett.* **2015**, *6* (19), 3781–3786. https://doi.org/10.1021/acs.jpclett.5b01666.

(28) Li, Z.; Kolodziej, C.; Zhang, T.; McCleese, C.; Kovalsky, A.; Zhao, Y.; Lambrecht, W. R. L.; Burda, C. Optoelectronic Dichotomy of Mixed Halide $CH_3NH_3Pb(Br_{1-x}Cl_x)_3$ Single Crystals: Surface versus Bulk Photoluminescence. *J. Am. Chem. Soc.* **2018**, *140* (37), 11811–11819. https://doi.org/10.1021/jacs.8b07560.

(29) García-Batlle, M.; Baussens, O.; Amari, S.; Zaccaro, J.; Gros-Daillon, E.; Verilhac, J.; Guerrero, A.; Garcia-Belmonte, G. Moving Ions Vary Electronic Conductivity in Lead Bromide Perovskite Single Crystals through Dynamic Doping. *Adv. Electron. Mater.* **2020**, *6* (10), 2000485. https://doi.org/10.1002/aelm.202000485.

(30) Zhang, X.; Li, L.; Sun, Z.; Luo, J. Rational Chemical Doping of Metal Halide Perovskites. *Chem. Soc. Rev.* **2019**, *48* (2), 517–539. https://doi.org/10.1039/C8CS00563J.

(31) Zhou, Y.; Chen, J.; Bakr, O. M.; Sun, H.-T. Metal-Doped Lead Halide Perovskites: Synthesis, Properties, and Optoelectronic Applications. *Chem. Mater.* **2018**, *30* (19), 6589–6613. https://doi.org/10.1021/acs.chemmater.8b02989.

(32) Euvrard, J.; Yan, Y.; Mitzi, D. B. Electrical Doping in Halide Perovskites. *Nat Rev Mater* **2021**, *6* (6), 531–549. https://doi.org/10.1038/s41578-021-00286-z.

(33) Shi, T.; Yin, W.-J.; Hong, F.; Zhu, K.; Yan, Y. Unipolar Self-Doping Behavior in Perovskite $CH_3NH_3PbBr_3$. *Appl. Phys. Lett.* **2015**, *106* (10), 103902. https://doi.org/10.1063/1.4914544.

(34) Wang, Q.; Shao, Y.; Xie, H.; Lyu, L.; Liu, X.; Gao, Y.; Huang, J. Qualifying Composition Dependent *p* and *n* Self-Doping in $CH_3NH_3PbI_3$. *Appl. Phys. Lett.* **2014**, *105* (16), 163508. https://doi.org/10.1063/1.4899051.

(35) Paul, G.; Chatterjee, S.; Bhunia, H.; Pal, A. J. Self-Doping in Hybrid Halide Perovskites via Precursor Stoichiometry: To Probe the Type of Conductivity through Scanning Tunneling Spectroscopy. *J. Phys. Chem. C* **2018**, *122* (35), 20194–20199. https://doi.org/10.1021/acs.jpcc.8b06968.

(36) Su, Z.; Chen, Y.; Li, X.; Wang, S.; Xiao, Y. The Modulation of Opto-Electronic Properties of CH3NH3PbBr3 Crystal. *J Mater Sci: Mater Electron* **2017**, *28* (15), 11053–11058. https://doi.org/10.1007/s10854-017-6889-3.

(37) McCluskey, M. D.; McCluskey, M. D.; Haller, E. E.; Haller, E. E. *Dopants and Defects in Semiconductors*, 2nd ed.; CRC Press: Boca Raton, 2018. https://doi.org/10.1201/b21986.

(38) Amari, S. Étude des matériaux pérovskites pour la détection directe des rayonnements ionisants. Ph.D. diss., Université Grenoble Alpes, Grenoble, France, 2020.

(39) INTERNATIONAL STANDARD IEC 62220-1 : Medical Electrical Equipment – Characteristics of Digital X-Ray Imaging Devices. International Electrotechnical Commission June 2007.

(40) Kasap, S.; Frey, J. B.; Belev, G.; Tousignant, O.; Mani, H.; Greenspan, J.; Laperriere, L.; Bubon, O.; Reznik, A.; DeCrescenzo, G.; Karim, K. S.; Rowlands, J. A. Amorphous and Polycrystalline Photoconductors for Direct Conversion Flat Panel X-Ray Image Sensors. *Sensors* **2011**, *11* (5), 5112–5157. https://doi.org/10.3390/s110505112.

(41) Baussens, O. Nouveau matériau pérovskite pour la radiographie médicale. Ph.D. diss., Université de Bordeaux, 2021.

(42) Mix, L. T.; Ghosh, D.; Tisdale, J.; Lee, M.-C.; O'Neal, K. R.; Sirica, N.; Neukirch, A. J.; Nie, W.; Taylor, A. J.; Prasankumar, R. P.; Tretiak, S.; Yarotski, D. A. Hot Carrier Cooling and Recombination Dynamics of Chlorine-Doped Hybrid Perovskite Single Crystals. *J. Phys. Chem. Lett.* **2020**, *11* (19), 8430–8436. https://doi.org/10.1021/acs.jpclett.0c02243.

(43) Hecht, K. Zum Mechanismus des lichtelektrischen Primärstromes in isolierenden Kristallen. *Z. Physik* **1932**, *77* (3–4), 235–245. https://doi.org/10.1007/BF01338917.

(44) Wei, H.; Fang, Y.; Mulligan, P.; Chuirazzi, W.; Fang, H.-H.; Wang, C.; Ecker, B. R.; Gao, Y.; Loi, M. A.; Cao, L.; Huang, J. Sensitive X-Ray Detectors Made of Methylammonium Lead Tribromide Perovskite Single Crystals. *Nature Photon* **2016**, *10* (5), 333–339. https://doi.org/10.1038/nphoton.2016.41.

(45) Stoumpos, C. C.; Malliakas, C. D.; Peters, J. A.; Liu, Z.; Sebastian, M.; Im, J.; Chasapis, T. C.; Wibowo, A. C.; Chung, D. Y.; Freeman, A. J.; Wessels, B. W.; Kanatzidis, M. G. Crystal Growth of the Perovskite Semiconductor CsPbBr3 : A New Material for High-Energy Radiation Detection. *Crystal Growth & Design* **2013**, *13* (7), 2722–2727. https://doi.org/10.1021/cg400645t.

(46) Many, A. High-Field Effects in Photoconducting Cadmium Sulphide. *Journal of Physics and Chemistry of Solids* **1965**, *26* (3), 575–578. https://doi.org/10.1016/0022-3697(65)90133-2.

(47) Ramo, S. Currents Induced by Electron Motion. *Proc. IRE* **1939**, *27* (9), 584–585. https://doi.org/10.1109/JRPROC.1939.228757.

(48) Venugopalan, V.; Sorrentino, R.; Topolovsek, P.; Nava, D.; Neutzner, S.; Ferrari, G.; Petrozza, A.; Caironi, M. High-Detectivity Perovskite Light Detectors Printed in Air from Benign Solvents. *Chem* **2019**, *5* (4), 868–880. https://doi.org/10.1016/j.chempr.2019.01.007.

(49) Baussens, O.; Maturana, L.; Amari, S.; Zaccaro, J.; Verilhac, J.-M.; Hirsch, L.; Gros-Daillon, E. An Insight into the Charge Carriers Transport Properties and Electric Field Distribution of $CH_3NH_3PbBr_3$ Thick Single Crystals. *Appl. Phys. Lett.* **2020**, *117* (4), 041904. https://doi.org/10.1063/5.0011713.

(50) Musiienko, A.; Ceratti, D. R.; Pipek, J.; Brynza, M.; Elhadidy, H.; Belas, E.; Betušiak, M.; Delport, G.; Praus, P. Defects in Hybrid Perovskites: The Secret of Efficient Charge Transport. *Adv. Funct. Mater.* **2021**, *31* (48), 2104467. https://doi.org/10.1002/adfm.202104467.

(51) Jia, S.; Xiao, Y.; Hu, M.; He, X.; Bu, N.; Li, N.; Liu, Y.; Zhang, Y.; Cui, J.; Ren, X.; Zhao, K.; Liu, M.; Wang, S.; Yuan, N.; Ding, J.; Yang, Z.; Liu, S. Ion-Accumulation-Induced Charge Tunneling for High Gain Factor in P–I–N-Structured Perovskite $CH_3NH_3PbI_3$ X-Ray Detector. *Adv. Mater. Technol.* **2021**, 2100908. https://doi.org/10.1002/admt.202100908.

(52) Duijnstee, E. A.; Ball, J. M.; Le Corre, V. M.; Koster, L. J. A.; Snaith, H. J.; Lim, J. Toward Understanding Space-Charge Limited Current Measurements on Metal Halide Perovskites. *ACS Energy Lett.* **2020**, *5* (2), 376–384. https://doi.org/10.1021/acsenergylett.9b02720.

(53) García-Batlle, M.; Mayén Guillén, J.; Chapran, M.; Baussens, O.; Zaccaro, J.; Verilhac, J.-M.; Gros-Daillon, E.; Guerrero, A.; Almora, O.; Garcia-Belmonte, G. Coupling between Ion Drift and Kinetics of Electronic Current Transients in $MAPbBr_3$ Single Crystals. *ACS Energy Lett.* **2022**, *7* (3), 946–951. https://doi.org/10.1021/acsenergylett.1c02578.

(54) Almora, O.; Matt, G. J.; These, A.; Kanak, A.; Levchuk, I.; Shrestha, S.; Osvet, A.; Brabec, C. J.; Garcia-Belmonte, G. Surface versus Bulk Currents and Ionic Space-Charge Effects

in $CsPbBr_3$ Single Crystals. *J. Phys. Chem. Lett.* **2022**, *13* (17), 3824–3830. https://doi.org/10.1021/acs.jpclett.2c00804.

(55) García-Batlle, M.; Deumel, S.; Huerdler, J. E.; Tedde, S. F.; Guerrero, A.; Almora, O.; Garcia-Belmonte, G. Mobile Ion-Driven Modulation of Electronic Conductivity Explains Long-Timescale Electrical Response in Lead Iodide Perovskite Thick Pellets. *ACS Appl. Mater. Interfaces* **2021**, *13* (30), 35617–35624. https://doi.org/10.1021/acsami.1c06046.

(56) Zanichelli, M.; Santi, A.; Pavesi, M.; Zappettini, A. Charge Collection in Semi-Insulator Radiation Detectors in the Presence of a Linear Decreasing Electric Field. *J. Phys. D: Appl. Phys.* **2013**, *46* (36), 365103. https://doi.org/10.1088/0022-3727/46/36/365103.

(57) Bertolini, G.; Coche, A. *Semiconductor Detectors*, Eds. Interscience.; Wiley, 1968.

(58) Wei, W.; Zhang, Y.; Xu, Q.; Wei, H.; Fang, Y.; Wang, Q.; Deng, Y.; Li, T.; Gruverman, A.; Cao, L.; Huang, J. Monolithic Integration of Hybrid Perovskite Single Crystals with Heterogenous Substrate for Highly Sensitive X-Ray Imaging. *Nature Photon* **2017**, *11* (5), 315–321. https://doi.org/10.1038/nphoton.2017.43.

(59) Xia, M.; Song, Z.; Wu, H.; Du, X.; He, X.; Pang, J.; Luo, H.; Jin, L.; Li, G.; Niu, G.; Tang, J. Compact and Large-Area Perovskite Films Achieved via Soft-Pressing and Multi-Functional Polymerizable Binder for Flat-Panel X-Ray Imager. *Adv Funct Materials* **2022**, 2110729. https://doi.org/10.1002/adfm.202110729.

(60) Kim, Y. C.; Kim, K. H.; Son, D.-Y.; Jeong, D.-N.; Seo, J.-Y.; Choi, Y. S.; Han, I. T.; Lee, S. Y.; Park, N.-G. Printable Organometallic Perovskite Enables Large-Area, Low-Dose X-Ray Imaging. *Nature* **2017**, *550* (7674), 87–91. https://doi.org/10.1038/nature24032.

(61) Zhang, H.; Wang, F.; Lu, Y.; Sun, Q.; Xu, Y.; Zhang, B.-B.; Jie, W.; Kanatzidis, M. G. High-Sensitivity X-Ray Detectors Based on Solution-Grown Caesium Lead Bromide Single Crystals. *J. Mater. Chem. C* **2020**, *8* (4), 1248–1256. https://doi.org/10.1039/C9TC05490A.

(62) Musiienko, A.; Moravec, P.; Grill, R.; Praus, P.; Vasylchenko, I.; Pekarek, J.; Tisdale, J.; Ridzonova, K.; Belas, E.; Landová, L.; Hu, B.; Lukosi, E.; Ahmadi, M. Deep Levels, Charge Transport and Mixed Conductivity in Organometallic Halide Perovskites. *Energy Environ. Sci.* **2019**, *12* (4), 1413–1425. https://doi.org/10.1039/C9EE00311H.

(63) Feng, Y.; Pan, L.; Wei, H.; Liu, Y.; Ni, Z.; Zhao, J.; Rudd, P. N.; Cao, L. R.; Huang, J. Low Defects Density $CsPbBr_3$ Single Crystals Grown by an Additive Assisted Method for Gamma-Ray Detection. *J. Mater. Chem. C* **2020**, *8* (33), 11360–11368. https://doi.org/10.1039/D0TC02706E.

(64) Du, X.; Liu, Y.; Pan, W.; Pang, J.; Zhu, J.; Zhao, S.; Chen, C.; Yu, Y.; Xiao, Z.; Niu, G.; Tang, J. Chemical Potential Diagram Guided Rational Tuning of Electrical Properties: A Case Study of $CsPbBr_3$ for X-ray Detection. *Advanced Materials* **2022**, 2110252. https://doi.org/10.1002/adma.202110252.

(65) Musiienko, A.; Pipek, J.; Praus, P.; Brynza, M.; Belas, E.; Dryzhakov, B.; Du, M.-H.; Ahmadi, M.; Grill, R. Deciphering the Effect of Traps on Electronic Charge Transport Properties of Methylammonium Lead Tribromide Perovskite. *Sci. Adv.* **2020**, *6* (37), eabb6393. https://doi.org/10.1126/sciadv.abb6393.

(66) Schlesinger, T. E.; James, R. B. *Semiconductors for Room Temperature Nuclear Detector Applications*, Academic Press.; Semiconductors and Semimetals; 1995; Vol. 43.

(67) Schlesinger, T. E.; Toney, J. E.; Yoon, H.; Lee, E. Y.; Brunett, B. A.; Franks, L.; James, R. B. Cadmium Zinc Telluride and Its Use as a Nuclear Radiation Detector Material. *Materials Science and Engineering: R: Reports* **2001**, *32* (4–5), 103–189. https://doi.org/10.1016/S0927-796X(01)00027-4.

(68) Kim, H.; Churilov, A.; Ciampi, G.; Cirignano, L.; Higgins, W.; Kim, S.; O'Dougherty, P.; Olschner, F.; Shah, K. Continued Development of Thallium Bromide and Related

Compounds for Gamma-Ray Spectrometers. *Nuclear Instruments and Methods in Physics Research Section A: Accelerators, Spectrometers, Detectors and Associated Equipment* **2011**, *629* (1), 192–196. https://doi.org/10.1016/j.nima.2010.10.097.

(69) Li, Y.; Adeagbo, E.; Koughia, C.; Simonson, B.; Pettipas, R. D.; Mishchenko, A.; Arnab, S. M.; Laperrière, L.; Belev, G.; Stevens, A. L.; Kasap, S. O.; Kelly, T. L. Direct Conversion X-Ray Detectors with 70 PA Cm $^{-2}$ Dark Currents Coated from an Alcohol-Based Perovskite Ink. *J. Mater. Chem. C* **2022**, *10* (4), 1228–1235. https://doi.org/10.1039/D1TC05338H.

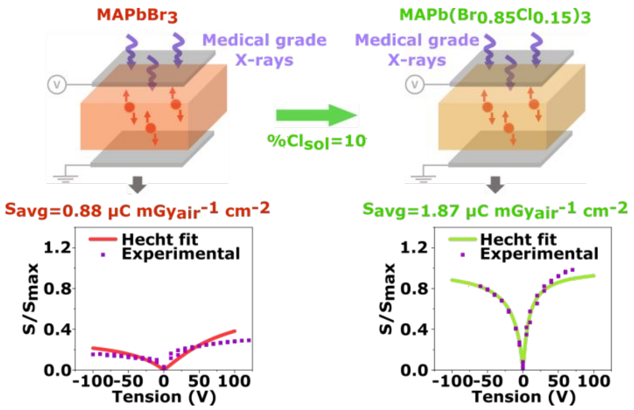
MAPbBr3
Medical grade X-rays
MAPb(Br0.85Cl0.15)3
Medical grade X-rays
V
%Clsol=10
V
Savg=0.88 µC mGyair-1 cm-2
Savg=1.87 µC mGyair-1 cm-2
Hecht fit
Experimental
S/Smax
1.2
0.8
0.4
0.0
-100-50 0 50 100
Tension (V)
Hecht fit
Experimental
S/Smax
1.2
0.8
0.4
0.0
-100-50 0 50 100
Tension (V)